ISSN (Print) 1226-1750
ISSN (Online) 2233-6656
Journal of Magnetics 30(4), 619-627 (2025) https://doi.org/10.4283/JMAG.2025.30.4.619

Usefulness Evaluation of Deep Learning Super Resolution Technique in Clinical Application of Image Guided Diagnosis and Treatment using Magnetic Resonance Imaging of Metastatic Brain Tumor

Jun-Ho Hwang[1], Kyung-Bae Lee[2], Ji-An Choi[3], and Chang Kyu Park[1,4]*

[1]*Department of Neurosurgery, Kyung Hee University Medical Center, Seoul 02447, Republic of Korea*
[2]*Department of Radiotechnology, Wonkwang Health Science University, Iksan 54538, Republic of Korea*
[3]*Department of Radiology, Kyung Hee University Medical Center, Seoul 02447, Republic of Korea*
[4]*Department of Neurosurgery, Kyung Hee University College of Medicine, Seoul 02447, Republic of Korea*

(Received 28 May 2025, Received in final form 4 November 2025, Accepted 5 November 2025)

This study aimed to implement artificial intelligence (AI) techniques using magnetic resonance imaging (MRI) of metastatic brain tumors for potential application in diagnosis and surgical environments. The experimental method involved reconstructing MRI data by applying an AI based super resolution (SR) technique to the ground truth (GT) images obtained using T2 weighted imaging (T2WI), T1 weighted imaging (T1WI), contrast enhanced T1WI (CE-T1WI), and contrast enhanced fluid attenuated inversion recovery (CE-FLAIR). The performance of the reconstructed images was evaluated based on peak signal to noise ratio (PSNR), structural similarity index measure (SSIM), and gamma knife radiosurgery (GKRS) coordinate systems. The results showed that the PSNR and SSIM values of the SR technique were higher than those achieved with conventional image post processing methods, and no differences were observed in the radiosurgery coordinates. Consequently, SR demonstrated superior image quality improvement without altering the coordinate system, confirming its utility as a viable technique for the diagnosis and surgical treatment of metastatic brain tumors.

Keywords : metastatic brain tumor, artificial intelligence (AI), deep learning, super resolution (SR), magnetic resonance imaging (MRI)

1. Introduction

Metastatic brain tumors are pathological conditions that arise when cancer cells spread from a primary lesion to the brain, significantly affecting motor function, cognitive abilities, and emotional stability, thereby diminishing patients' quality of life [1, 2]. Accordingly, treatment strategies are established based on factors such as tumor size, location, and the patient's overall condition, and may include pharmacological therapy, surgical resection, or stereotactic radiosurgery (SRS) [3, 4]. In particular, gamma knife radiosurgery (GKRS) serves as a non-invasive alternative for patients who are not suitable candidates for surgery or who exhibit limited response to medications, delivering highly focused gamma rays to the lesion with demonstrated therapeutic efficacy [5, 6].

The success of GKRS critically depends on the establishment of a precise treatment plan based on high-resolution imaging, in which magnetic resonance imaging (MRI) plays a central role by providing accurate three-dimensional spatial information about the lesion [6-8]. Various MRI techniques such as T1 weighted imaging (T1WI), T2 weighted imaging (T2WI), time of flight (TOF), and diffusion weighted imaging (DWI) offer visual representations of the radiological characteristics of lesions, and the utility of post-processing methods to enhance image quality has also been reported [9-12]. However, acquiring high-resolution MRI requires prolonged scan times, which increases the risk of motion artifacts. Furthermore, if post-processing techniques distort the structural integrity of the original image (ground truth), diagnostic and therapeutic accuracy may be compromised.

To overcome these limitations, super resolution (SR) techniques have gained attention [13-15]. SR is an image reconstruction method based on artificial intelligence (AI)

---

*Corresponding author: Tel: +82-2-958-8385
Fax: +82-2-958-8380, e-mail: changchaz@naver.com

that learns patterns and fine details from low-resolution images to generate high-resolution counterparts, with strong performance in preserving the texture characteristics of the original images without distortion [16-19]. Given that metastatic brain tumors exhibit distinct texture characteristics compared to normal tissue, SR techniques can facilitate more precise visualization of lesions and surrounding structures, thereby contributing to improved diagnostic accuracy and radiation treatment planning.

This study aims to apply a deep learning based SR technique to MRI of metastatic brain tumors, evaluate the degree of image quality enhancement, and analyze the impact of the reconstructed images on GKRS coordinate system configuration. Through this investigation, we seek to explore the clinical applicability of SR technology and provide evidence for its potential to improve the precision of GKRS in future clinical practice.

2. Materials and Methods

2.1. Image data

The data used in this study consist of MRI scans from 30 patients (15 males and 15 females) who were diagnosed with metastatic brain tumors and underwent GKRS at our institution between December 2020 and October 2024.

Fig. 1 presents representative MRI data of a brain tumor obtained for GKRS. The MRI examination for GKRS was conducted using a non-frame-based approach. Images were acquired using a Philips Intra Achieva 3.0 Tesla MRI equipped with a SENSE_NEURO_VASC multi-channel head coil, and included T2WI, T1WI, contrast enhanced T1WI (CE-T1WI), and contrast enhanced fluid attenuated inversion recovery (CE-FLAIR). All imaging data were retrospectively collected following prior approval from the institutional review board (IRB approval number: 2022-06-035).

Table 1 summarizes the composition of the dataset and the MRI acquisition parameters used. The entire dataset consists of 830 images with 16 bits, including 180 images of T2WI, 180 images of T1WI, 233 images of CE-T1WI, and 237 images of CE-FLAIR. To ensure consistency in image quality, identical imaging parameters were applied across all acquisitions.

2.2. Super resolution algorithm

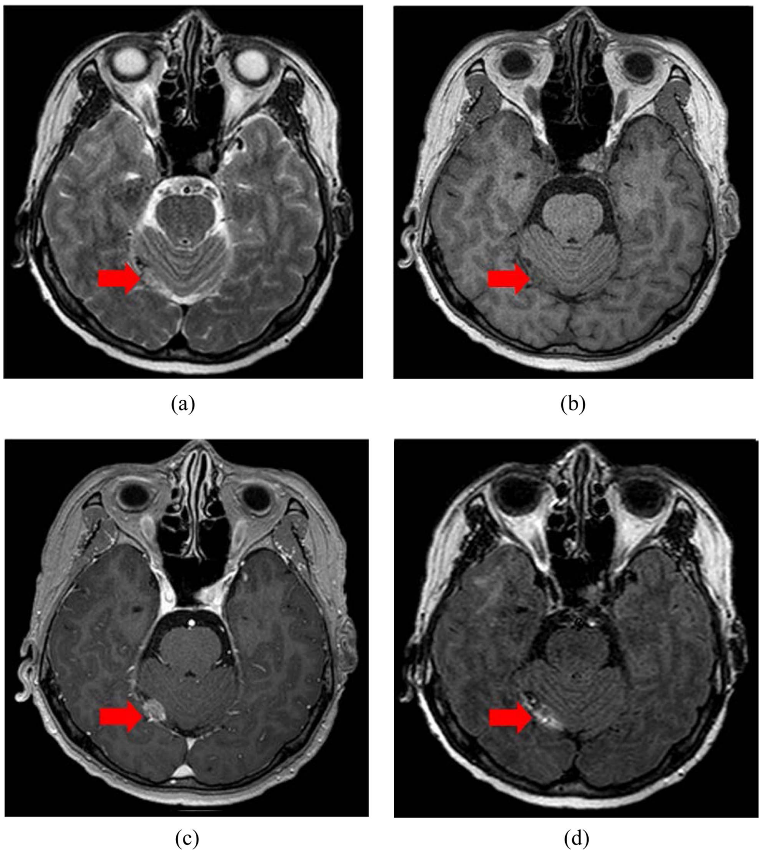
(a) (b)

(c) (d)

Fig. 1. (Color online) (a)–(d) represent MRI data of metastatic brain tumors and the red arrows indicate the locations of the metastatic lesions. (a) shows T2WI, (b) shows T1WI, (c) shows CE-T1WI, and (d) shows CE-FLAIR.

Table 1. Examination parameters.

MRI methods	Pulse Sequence	Slice thickness (mm)	Acquisition matrix	Recovery time (msec)	Echo time (msec)	Number of excitations	Flip angle (o)
T2WI	2D turbo spin echo	1	256 × 256	2500	110	1	-
T1WI	3D turbo field echo			5	2.5	1	8
CE-T1WI						2	
CE-FLAIR	Inversion recovery turbo spin echo			10000	120	1	90

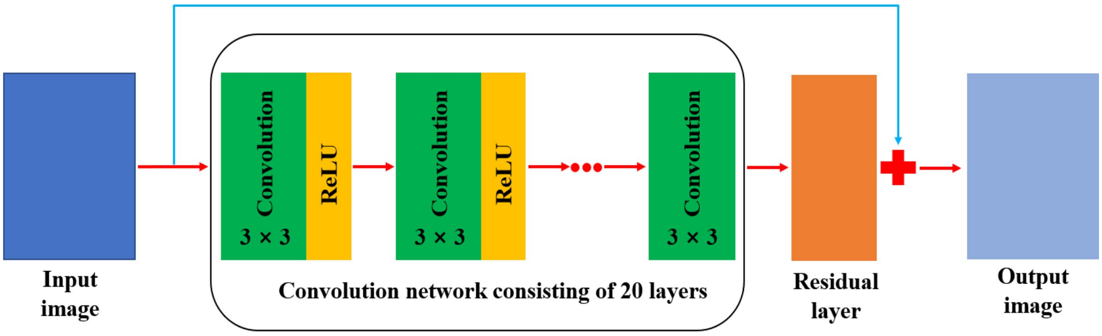

Fig. 2. (Color online) A schematic diagram of the algorithm for SR of the MRI dataset. It illustrates the process where the input image passes through convolutional and residual layers to be reconstructed, and the reconstructed MRI data are output by combining the residual image with the processed input.

The algorithm used to implement SR was the very deep super resolution (VDSR) algorithm. Fig. 2 shows the schematic of the VDSR algorithm, which implements SR based on low-resolution images, high-resolution images, and residual images.

The algorithm for implementing SR utilizes the VDSR algorithm. Let the dataset be N, the low resolution images be A, and the high-resolution images be B. The dataset can then be expressed as Equation (1):

$$\{A^{(i)}, B^{(i)}\}_{i=1}^{N} \tag{1}$$

The SR algorithm aims to reconstruct high-resolution images using training data. The algorithm predicts results through learning, where the network's prediction is denoted as f, and the reconstructed high resolution image is $\bar{B}$. This relationship is defined by Equation (2):

$$\bar{B} = \mathrm{f(X)} \tag{2}$$

The VDSR algorithm defines the residual image R based on the observation that most components of the input and output data are similar. R is defined by Equation (3):

$$\mathrm{R = B - X} \tag{3}$$

The loss function, L, which measures the difference between the residual image and the network prediction, L is given by Equation (4):

$$\mathrm{L} = \frac{1}{2}|R - f(X)|^2 \tag{4}$$

Table 2 outlines the configuration of the environment used for implementing the SR algorithm. The VDSR algorithm was implemented using MATLAB 2023a (MathWorks, USA) with the Parallel Computing Toolbox, Image Processing Toolbox, and Deep Learning Toolbox. The specifications of the computational setup are as follows: Operating System: Windows 11 Education. central processing unit (CPU): Intel Core i9–12900KF. graphics processing unit (GPU): GeForce RTX 3080.

Table 2. Computer setting.

System environments	Computer specifications
Computer language	MATLAB 2023a
Dataset processing and computation	Parallel computing toolbox
Deep learning implementation	Deep learning tool box
Image processing	Image processing toolbox
Operating system	Windows 11 education
Central processing unit	Intel core i9 – 12900KF
Graphic processing unit	GeForce RTX 3080

2.3. Dataset pre processing

The MRI data of metastatic brain tumors were transmitted to the picture archiving and communication system (PACS) and downloaded in the digital imaging and communications in medicine (DICOM) format with no compression. Subsequently, the DICOM data were converted into the joint photographic experts group (JPEG) format with 8 bit processing, and the input resolution was normalized to 256 × 256.

2.4. Setting up the training dataset

First, the GT images were converted into the YCbCr color space, consisting of luminance (Y channel) and chrominance (Cb and Cr channels). To create low resolution sample images, the size of the Y channel was reduced and then resized back to the original dimensions using bicubic interpolation. The training dataset was defined as pairs of up-sampled images and their corresponding residual images. The up-sampled images and their computed residual images were saved in a predefined directory for training purposes.

2.5. Training options

Table 3 outlines the training options used for the algorithm. To optimize SR performance for clinical imaging, various training configurations were empirically tested, and the condition that demonstrated the best performance was adopted in this study. The optimizer used was stochastic gradient descent with momentum (SGDM), which has proven effective for assessing the generalized performance of learning models and enables stable training. Incorporating momentum helps regulate the degree of gradient descent during training and mitigates issues related to local minima. A momentum value of 0.9 was employed, as it is commonly accepted as a stable and empirically validated parameter, and yielded stable training results in this study as well. Regarding the initial learning rate, it was found that excessively low values significantly slowed the training process. In preliminary experiments, a learning rate of 0.01 resulted in overly slow convergence. Therefore, the initial learning rate was set to 0.1, with a scheduled decrease over time as training progressed. The L2 regularization factor was included to prevent model overfitting. An initial search was conducted within the range of 0.0001 to 0.0005, and the final value was set to 0.0001. Additionally, to prevent premature convergence and potential overfitting, the number of training epochs was set to 100. The mini batch size was empirically set to 32, a commonly used value for evaluating generalized model performance. Finally, the training loss rate was visualized as a curve to assess model performance throughout the learning process.

Table 3. Option setting.

Options	Parameters	Setting value
Training options	Optimizer	Stochastic gradient descent with momentum
	Momentum	0.9
	Initial learning rate	0.1
	Learning rate factor	0.1
	L2 regularization	0.0001
	Gradient Threshold	0.01
	Gradient threshold method	Learn rate drop factor
	Learn rate drop factor	10
Mini batch options	Max epoch	100
	Mini batch size	32

2.6. Implementation of super resolution algorithm

The algorithm layers for implementing SR on MRI data were configured. The structure consisted of an input layer, a convolution layer, a rectified linear unit (ReLU) layer, and an output layer, which were combined to construct the VDSR model. For SR implementation based on the VDSR algorithm, low resolution images generated through sampling were resized to the GT dimensions and converted to the YCbCr color space. Bicubic interpolation was applied to each channel. Subsequently, the Y channel was isolated and input into the VDSR model to generate the residual image. The high resolution Y component was obtained by combining the output residual image with the Y channel. Finally, the high resolution Y component was merged with the remaining chrominance channels to produce the SR based high resolution MRI data.

2.7. Image quality and coordinate evaluation

The performance of the SR method was evaluated using the peak signal to noise ratio (PSNR) and structural similarity index measure (SSIM). To assess statistical significance, a paired t-test was conducted using MATLAB, and a p-value of less than 0.05 was considered statistically significant. The coordinate system for GKRS was evaluated based on the 4 mm shot of the tissue maximum ratio (TMR) 10 dose algorithm in Leksell Gamma Plan 11.4.2 (Elekta, Sweden) when applied to metastatic brain tumors.

3. Results

3.1. Training options

The VDSR algorithm was trained over a total of 100 epochs, and the training loss curve is presented in Fig. 3.

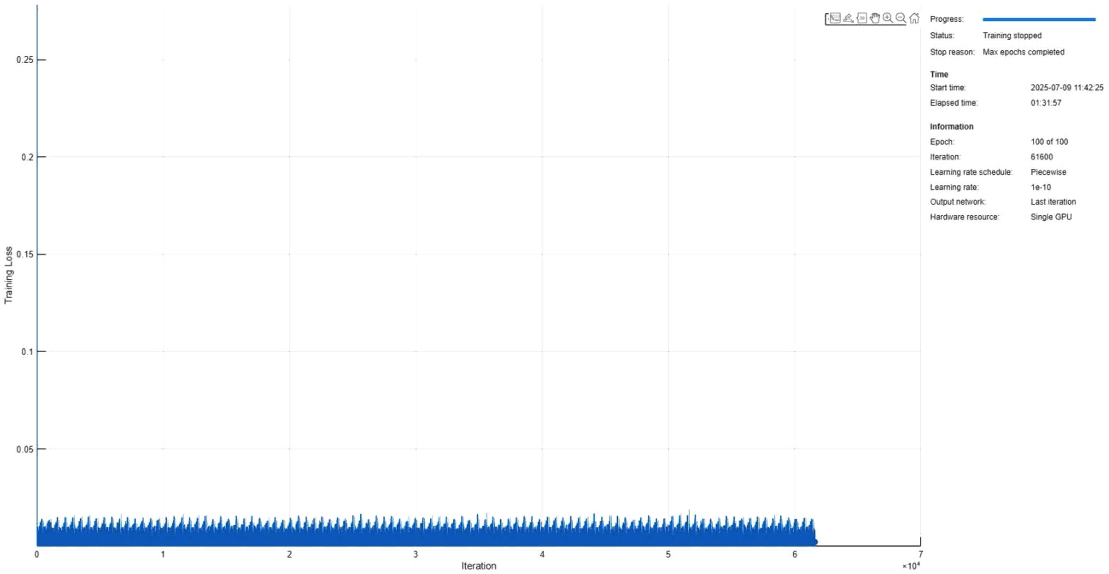

Progress:
Status: Training stopped
Stop reason: Max epochs completed

Time
Start time: 2025-07-09 11:42:25
Elapsed time: 01:31:57

Information
Epoch: 100 of 100
Iteration: 61600
Learning rate schedule: Piecewise
Learning rate: 1e-10
Output network: Last iteration
Hardware resource: Single GPU

Fig. 3. (Color online) Graph representing the loss rate of the VDSR algorithm. The curve demonstrates a rapid initial decrease in loss, followed by a gradual plateau, indicating convergence stability.

The loss rapidly decreased during the initial phase of training and then showed stable convergence.

3.2. Implementation of super resolution algorithm

Table 4 outlines the layer composition of the VDSR algorithm. In the input layer, the patch size of the input

Table 4. VDSR algorithm.

Algorithm	Layer setting
Input layer	41 × 41 × 1 (Y channel)
Convolution layer	3 × 3 filter operation
ReLU layer	Activation function
Output layer	Replacement of regression layer

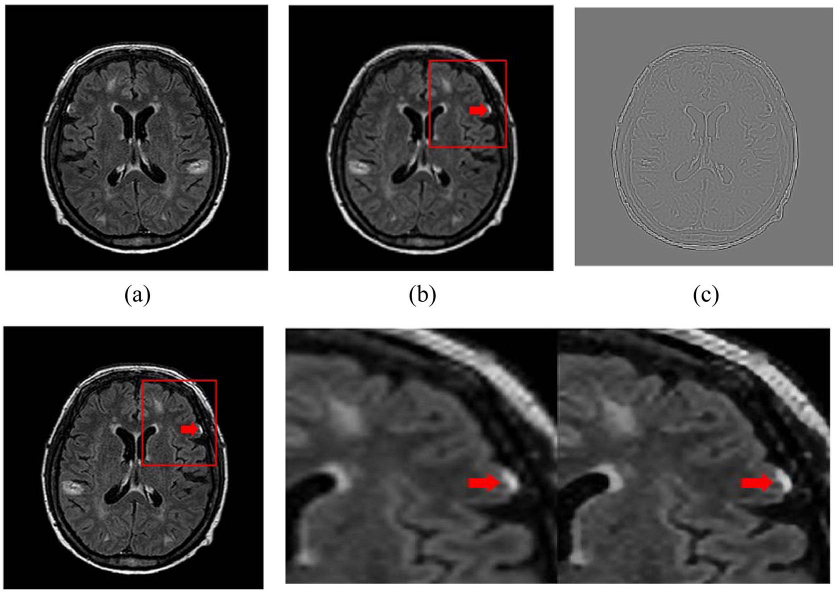
(a) (b) (c)
(d) (e)

Fig. 4. (Color online) (a)–(e) illustrate the SR process for generating high resolution images using the GT, low resolution images, and residual images of CE-FLAIR. (a) represents the GT, (b) shows the low resolution image, (c) depicts the residual image, (d) displays the SR based high resolution image, and (e) provides a magnified comparison of the metastatic brain tumor between (b) (left: low-resolution) and (d) (right: SR-based high-resolution). The red arrows indicated in the figure mean the location of the metastatic brain tumor, and the red box is an enlarged area of (e).

Table 5. Image quality evaluation.

Dataset	Scale factor	*PSNR (db)		**SSIM	
		Bicubic interpolation	Super resolution	Bicubic interpolation	Super resolution
MRI data	× 2	30.4	32.6	0.93	0.95
	× 3	27.7	30.4	0.88	0.90
	× 4	26.6	28.4	0.85	0.88

*, **$p<0.05$

data was set to 41 × 41 to enable the 20 layers of the VDSR algorithm to perform patch based computations. Due to the algorithm's use of luminance components, the Y component was specifically designated, resulting in a final input layer size of 41 × 41 × 1 channels. In the convolution layer, the learning process employed 3 × 3 filters configured into 64 units, with each operation activated in the ReLU layer. The output layer was replaced with a regression layer to estimate the error between the residual image and the network prediction.

The MRI data were converted into YCbCr channels, as shown in Fig. 4. Among these, the Y channel of the data was passed to the network to generate the residual image. Finally, the high-resolution Y channel was combined with the remaining color channels to produce the MRI data with SR applied.

3.3. Image quality and coordinate evaluation

Table 5 presents the results of PSNR and SSIM evaluations. Image quality was highest when the scale factor was 2, as the PSNR and SSIM of the MRI data reached their peak values, showing statistically significant differences. Furthermore, although SSIM varied depending on the scale factor, the radiosurgery coordinates of the MRI data reconstructed using the SR algorithm showed no changes compared to the GT.

4. Discussions

The American Association of Physicists in Medicine (AAPM) has proposed guidelines for maintaining stable image quality [20-22]. The core of these guidelines emphasizes quality assurance (QA) of imaging equipment and the application of appropriate imaging parameters, specifying the need to effectively manage factors that degrade image resolution [21]. Even when QA and proper imaging conditions are implemented, random resolution degradation within images can be addressed and improved through post-processing techniques [9-11]. However, post-processing techniques often lead to loss of original data, resulting in image distortion. In many cases, the benefits obtained from applying post-processing techniques are outweighed by the disadvantages caused by distortion [12, 23]. Consequently, there is a limitation in the increasing loss rate of image information. This suggests that conventional methods may not be the optimal approach to managing image quality, highlighting the need for new methods that can maintain image quality while minimizing data distortion. This study aims to address these issues by applying SR techniques to simultaneously achieve stable improvements in image quality and minimize data loss. Furthermore, it evaluates how these methods can be utilized in clinical environments where image guidance is essential.

It was first necessary to select an AI algorithm suitable for the research objective. AI algorithms learn and compute complex patterns from input data, and their pattern processing speed and utilization of computational resources vary depending on the type of algorithm [23-25]. In this context, denoising techniques can be considered as one category of AI-based methods for enhancing image resolution due to their shared objective of improving image quality. Denoising focuses on removing noise from images and has demonstrated strong performance in enhancing image clarity. While it involves preservation and partial restoration of texture components, texture recovery remains a secondary objective in denoising. In contrast, SR techniques are designed to reconstruct fine texture details lost due to low resolution, while also performing noise reduction as a secondary effect. Since the primary aim of this study was to enhance spatial resolution and restore fine textures rather than simply reduce noise, a SR algorithm was employed in the experiments.

Representative SR algorithms designed to enhance image resolution include super resolution convolutional neural network (SRCNN), VDSR, and enhanced deep super resolution (EDSR) [24-26]. SRCNN is one of the earliest convolutional neural network (CNN) based SR algorithms, characterized by a relatively simple architecture. However, due to its shallow depth, its learning capacity is limited, and its performance in improving image quality is relatively constrained. Moreover, the inherently low learning rate of SRCNN reduces its efficiency in practical applications [24]. VDSR, on the other hand, consists of 20 deep convolutional layers, enabling superior performance in image quality enhancement compared to earlier models. It also allows for higher learning rates, facilitating faster and more effective training [24, 25]. EDSR, which was proposed after VDSR, adopts a deeper residual learning-based architecture and demonstrates improved reconstruction of high-frequency image details. By eliminating batch normalization layers, EDSR further enhances both training stability and overall performance [26]. However, EDSR requires greater computational resources and memory, and it necessitates separate training for each upscaling factor, which poses limitations for deployment in clinical environments with restricted computational capacity. Considering these factors, this study adopted VDSR as the SR algorithm for image quality enhancement, based on its structural simplicity, clinical applicability, and training stability.

The VDSR algorithm used in this study was trained over a total of 100 epochs. The training loss decreased sharply during the initial epochs and gradually converged in a stable manner after approximately 30 epochs. This convergence trend indicates that the model achieved sufficiently stable learning with respect to the training data. In other words, such convergence behavior supports the model's training stability and reproducibility of performance. The VDSR based SR algorithm implemented in this study utilized high resolution MRI datas that were first converted into the YCbCr color space, and only the Y channel-representing luminance information-was extracted and used for training. VDSR inherently performs SR on the Y channel after converting input images into the YCbCr space. Since the human visual system is significantly more sensitive to luminance than chrominance, applying SR to the Y channel has the greatest impact on perceived image quality. During training, the extracted Y channel was divided into 41 × 41 pixels patches to serve as inputs. This patch based approach enables the model to focus on reconstructing localized structures and is a standard implementation method for VDSR, balancing memory efficiency and training stability. Accordingly, in this study, special attention was given to verifying whether MRI data were correctly converted to the YCbCr color space and whether the Y channel was accurately processed by the algorithm without data loss. It was confirmed that both the up-sampled MRI data and residual learning outputs were successfully generated and saved to their designated directories, indicating that the metastatic brain tumor MRI data were correctly transformed into YCbCr format and that VDSR-based residual learning was properly implemented. Experimental results using the test dataset showed that the algorithm successfully generated residual images and reconstructed the super-resolved output effectively. Although the residual learning structure inherently produced some degree of noise suppression during the high-resolution detail reconstruction, this was considered a secondary effect. Notably, this study did not employ a stitching method to reassemble patch based outputs. To minimize the risk of aliasing artifacts that can arise during patch sampling and reconstruction, low resolution images were directly generated from high-resolution ground truth MRI data [27]. Furthermore, since the original images were acquired using a 3.0T MRI system under uniform imaging parameters, any potential aliasing effects were deemed negligible and not influential on the experimental results.

The resulting PSNR and SSIM provided significant insights for the study. First, compared to image post-processing techniques, the VDSR algorithm showed higher PSNR values across all scale factors, demonstrating superior image quality improvement, which was also statistically significant. One of the common issues with deep neural networks is the reduction in the size of feature maps as they pass through convolutional layers, leading to the loss of pixel information containing meaningful data. However, this algorithm applied padding to preserve pixel information [24, 25]. The consistently high PSNR values across all scale factors reflect this feature of the algorithm. A similar trend was observed in SSIM.

A previous study using MRI data from patients with trigeminal neuralgia demonstrated meaningful SR outcomes based on 2D fast spin echo sequences. In contrast, the present study utilized 3D turbo field echo sequences and focused on solid metastatic brain tumors-lesions that are commonly encountered in actual clinical practice. Accordingly, differences exist in both the imaging sequence and the target pathology. Unlike cranial nerve structures, metastatic brain tumors exhibit diverse morphologies and poorly defined boundaries, with tissue characteristics that are fundamentally different. Therefore, it is reasonable to expect that SR results in this context may differ from those obtained in studies targeting neural structures. Within this framework, the high SSIM values achieved by the VDSR algorithm in this study suggest that it effectively preserved and reconstructed the intrinsic texture features of metastatic brain tumors during the image reconstruction process. The high SSIM values recorded by the VDSR algorithm suggest that it effectively reconstructed and restored the unique texture components of metastatic brain tumors during the image reconstruction process. Notably, despite variations in SSIM across scale factors, there were no differences in the radiosurgery system coordinates, indicating that GKRS targeting was unaffected. In summary, this study achieved the following key outcomes: (1) SR techniques applied to MRI data provided consistent results even with test data outside the training dataset; (2) SR was successfully implemented for MRI data of metastatic brain tumors, significantly improving PSNR; (3) the VDSR algorithm effectively reconstructed and restored the texture components of metastatic brain tumors; and (4) despite SSIM not reaching 1, the consistency of radiosurgery coordinates between GT and reconstructed images confirms the feasibility of GKRS targeting. These findings highlight the success and clinical applicability of this study.

However, this study has certain limitations in terms of MRI data handling and computational resources. First, due to practical constraints related to computational capacity and storage, the original DICOM images were converted to 8-bit JPEG format for analysis. This conversion reduces the dynamic range of the images, which may affect the preservation of subtle anatomical details, such as tumor boundaries, and could limit the diagnostic utility of the reconstructed images to some extent [27-30]. In future studies, it would be beneficial to construct a training environment based on raw DICOM data and to incorporate preprocessing steps such as intensity normalization and window level adjustment. These enhancements are expected to further improve the clinical applicability of SR techniques.

Second, because the clinical data used in this study were retrospectively collected under IRB approval, the absolute number of metastatic brain tumor MRI cases was limited. This limitation may affect the generalizability of the SR algorithm's performance and raises the potential risk of overfitting [27-29]. Future studies should incorporate a broader range of imaging modalities and larger, more diverse datasets to validate and enhance the robustness of the proposed approach.

Third, due to limitations in available computational resources, this study employed the VDSR algorithm rather than more recent or advanced SR methods. Although VDSR offers a balance between performance and computational efficiency, recently proposed high performance SR models have shown considerable promise in further improving image quality. Therefore, if sufficient computational power and time become available in the future, it would be worthwhile to explore and apply these state-of-the-art algorithms. It should be noted, however, that introducing new algorithmic architectures or mathematical models that have not been pre-trained may lead to issues such as overfitting or slower convergence during training. Nevertheless, with adequate time and computational capacity, these approaches could be progressively investigated in future work.

And then, although the reconstructed images from the SR algorithm showed SSIM values exceeding 0.88 when compared to the GT, the differences introduced during the reconstruction process were not clearly explained [31, 32]. The VDSR algorithm used in this study is a regression based neural network architecture designed to reconstruct high resolution images from single low resolution inputs. Internally, it operates by repeatedly applying 3 × 3 convolutional layers and ReLU activation functions to minimize pixel wise differences between the input and target images. Unlike classification or object detection tasks, VDSR does not involve explicit attention maps or decision boundaries, which poses inherent limitations for the direct application of explainable AI techniques. As a result, in the context of radio surgical planning, reconstructed images should be used as auxiliary information, and the interpretation of data transformations during the reconstruction process must be supported by both AI-based analytical methods and clinical expertise [32-34]. Furthermore, additional experiments applying various gamma knife treatment plans are warranted to enhance the reliability and clinical relevance of the study's findings.

5. Conclusions

Despite these limitations, this study holds significant value in effectively improving the image quality of MRI data and quantitatively analyzing its potential application in the GKRS environment. These findings can serve as foundational data for the future clinical adoption of AI-based image reconstruction techniques in image-guided surgical environments.

References

[1] G. Tanzhu, L. Chen, J. Ning, W. Xue, C. Wang, G. Xiao, J. Yang, and R. Zhou, Med. Comm. **6**, e70020 (2025).

[2] E. R. Gerstner and R. L. Fine, JCO. **25**, 2306 (2007).

[3] K. R. Cho, M. H. Lee, D. S. Kong, H. J. Seol, D. H. Nam, J. M. Sun, J. S. Ahn, M. J. Ahn, K. C. Park, S. T. Kim, D. H. Lim, and J. I. Lee, J. Neurooncol. **125**, 331 (2015).

[4] S. Matsunaga, T. Shuto, and M. Sato, World Neurosurg. **89**, 455 (2016).

[5] C. C. Wu, W. Y. Guo, W. Y. Chung, H. M. Wu, C. J. Lin, C. C. Lee, K. D. Liu, and H. C. Yang, J. Neurosurg. **127**,

1384 (2017).

[6] A. G. Loganathan, M. D. Chan, N. Alphonse, A. M. Peiffer, A. J. Johnson, K. P. McMullen, J. J. Urbanic, P. A. Saconn, J. D. Bourland, M. T. Munley, E. G. Shaw, S. B. Tatter, and T. L. Ellis, J. Med. Imaging Radiat. Oncol. **56**, 554 (2012).

[7] T. Yousaf, G. Dervenoulas, and M. Politis, Int. Rev. Neurobiol. **141**, 31 (2018).

[8] S. L. Stuckey, T. D. Goh, T. Heffernan, and D. Rowan, AJR. **189**, 913 (2007).

[9] M. J. Donahue, M. R. Juttukonda, and J. M. Watchmaker, Neuroimage **154**, 43 (2017).

[10] R. Krissak, C. A. Mistretta, T. Henzler, A. Chatzikonstantinou, J. Scharf, S. O. Schoenberg, and C. Fink, PLoS One **6**, e17098 (2011).

[11] J. Mohan, V. Krishnaveni, and Y. Guo, Biomed. Signal Process Control **9**, 56 (2014).

[12] J. Schulz-Menger, D. A. Bluemke, J. Bremerich, S. D. Flamm, M. A. Fogel, M. G. Fridrich, R. J. Kim, F. V. Knobelsdorff-Brenkenhoff, C. M. Kramer, D. J. Pennell, S. Plein, and E. Nagel, J. Cardiovasc. Magn. Reson. **22**, 19 (2020).

[13] M. Tateishi, T. Nakaura, M. Kitajima, H. Uetani, M. Nakagawa, T. Inoue, J. I. Kuroda, A. Mukasa, and Y. Yamashita, J. Neurol. Sci. **410**, 116514 (2020).

[14] J. H. Hwang, C. K. Park, S. B. Kang, M. K. Choi, and W. H. Lee, Life **14**, 355 (2024).

[15] J. Zhu, C. Tan, J. Yang, G. Yang, and P. Lio, Int. J. Neural Syst. **31**, 2150037 (2021).

[16] M. Hou, L. Zhou, and J. Sun, Eur. Radiol. **33**, 1 (2023).

[17] Y. Liu, H. Zheng, Z. Liang, Q. Miao, W. G. Brisbane, L. S. Marks, S. S. Raman, R. E. Retier, G. Yang, and K. H. Sung, Diagnostics **11**, 1785 (2021).

[18] K. Schawkat, A. Ciritsis, U. S. Von, H. Honcharova-Biletska, C. Junhst, A. Weber, C. Gubler, J. Mertens, and C. S. Reiner, Eur. Radiol. **30**, 4675 (2020).

[19] S. Yuan, Y. Liu, R. Wei, J. Zhu, K. Men, and J. Dai, Med. Phys. **51**, 2695 (2024).

[20] C. K. Glide-Hurst, E. S. Paulson, K. McGee, N. Tyagi, Y. Hu, J. Balter, and J. Bayouth, Med. Phys. **48**, e636 (2021).

[21] R. R. Price, L. Axel, T. Morgen, R. Newman, W. Perman, N. Schneiders, M. Selikson, M. Wood, and S. R. Thomas, Med. Phys. **17**, 287 (1990).

[22] N. Yanasak, G. Clarke, R. J. Stafford, F. Goerner, M. Steckner, I. Bercha, J. Och, and M. Amurao, Parallel Imaging in MRI: Technology, Applications, and Quality Control, AAPM. America (2015).

[23] T. W. Wang, M. S. Hsu, W. K. Lee, H. C. Pan, H. C. Yang, C. C. Lee, and Y. T. Wu, Radiotherapy Oncol. **190**, 110007 (2024).

[24] J. W. Kim, J. K. Lee, and K. M. Lee, Proceedings of the IEEE Conference on Computer Vision and Pattern Recognition. arXiv. **1511.04045**, 1 (2016).

[25] S. Hitawala, Y. Li, X. Wang, and D. Yang, arXiv preprint. arXiv. **1810.05731**, 1 (2018).

[26] J. Grover, P. Liu, B. Dong, S. Shan, B. Whelan, P. Keall, and D. E. J. Waddington, Commun. Med. **4**, 64 (2024).

[27] C. Zhao, M. Shao, A. Carass, H. Li, B. E. Dewey, L. M. Ellingsen, J. Woo, M. A. Guttman, A. M. Blitz, M. Stone, P. A. Calabresi, H. Halperin, and J. L. Prince, Magn. Reson. Imaging **64**, 132 (2019).

[28] M. Xiao, Y. Wu, G. Zuo, S. Fan, H. Yu, Z. A. Shaikh, and Z. Wen, Wirel. Commun. Mob. Comput. **2021**, 1 (2021).

[29] M. M. Bejani and M. Ghatee, Artif. Intell. Rev. **54**, 6391 (2021).

[30] X. Zeke, H. Fengxiang, F. Shaopeng, S. Issei, T. Dacheng, and S. Masashi, Neural Comput. **33**, 2163 (2021).

[31] Y. LeCun, Y. Bengio, and G. Hinton, Nature **521**, 436 (2015).

[32] C. Rudin, Nat. Mach. Intell. **1**, 206 (2019).

[33] K. D. Apostolidis and G. A. Papakostas, Electronics **10**, 2132 (2021).

[34] S. Lin, L. Li, H. Zou, Y. Xu, and L. Lu, J. Med. Internet. Res. **24**, e40249 (2022).